

# A galaxy lacking dark matter

Pieter van Dokkum<sup>1</sup>, Shany Danieli<sup>1</sup>, Yotam Cohen<sup>1</sup>, Allison Merritt<sup>1,2</sup>, Aaron J. Romanowsky<sup>3,4</sup>, Roberto Abraham<sup>5</sup>, Jean Brodie<sup>4</sup>, Charlie Conroy<sup>6</sup>, Deborah Lokhorst<sup>5</sup>, Lamiya Mowla<sup>1</sup>, Ewan O’Sullivan<sup>6</sup>, Jielai Zhang<sup>5</sup>

<sup>1</sup>*Astronomy Department, Yale University, New Haven, CT 06511, USA*

<sup>2</sup>*Max-Planck-Institut für Astronomie, Königstuhl 17, D-69117 Heidelberg, Germany*

<sup>3</sup>*Department of Physics and Astronomy, San José State University, San Jose, CA 95192, USA*

<sup>4</sup>*University of California Observatories, 1156 High Street, Santa Cruz, CA 95064, USA*

<sup>5</sup>*Department of Astronomy & Astrophysics, University of Toronto, 50 St. George Street, Toronto, ON M5S 3H4, Canada*

<sup>6</sup>*Harvard-Smithsonian Center for Astrophysics, 60 Garden Street, Cambridge, MA, USA*

**Studies of galaxy surveys in the context of the cold dark matter paradigm have shown that the mass of the dark matter halo and the total stellar mass are coupled through a function that varies smoothly with mass. Their average ratio  $M_{\text{halo}}/M_{\text{stars}}$  has a minimum of about 30 for galaxies with stellar masses near that of the Milky Way (approximately  $5 \times 10^{10}$  solar masses) and increases both towards lower masses and towards higher masses.<sup>1,2</sup> The scatter in this relation is not well known; it is generally thought to be less than a factor of two for massive galaxies but much larger for dwarf galaxies.<sup>3,4</sup> Here we report the radial velocities of ten luminous globular-cluster-like objects in the ultra-diffuse galaxy<sup>5</sup> NGC1052–DF2, which has a stellar mass of approximately  $2 \times 10^8$  solar masses. We infer that its velocity dispersion is less than 10.5 kilometres per second with 90 per cent confidence, and we determine from this that its total mass within a radius of 7.6 kiloparsecs is less than  $3.4 \times 10^8$  solar masses. This implies that the ratio  $M_{\text{halo}}/M_{\text{stars}}$  is of order unity (and consistent with zero), a factor of at least 400 lower than expected.<sup>2</sup> NGC1052–DF2 demonstrates that dark matter is not always coupled with baryonic matter on galactic scales.**

NGC1052–DF2 was identified with the Dragonfly Telescope Array<sup>6</sup> in deep, wide-field imaging observations of the NGC 1052 group. The galaxy is not a new discovery; it was cataloged previously in a visual search of digitized photographic plates.<sup>7</sup> It stood out to us because of the remarkable contrast between its appearance in Dragonfly images and Sloan Digital Sky Survey (SDSS) data: with Dragonfly it is a low surface brightness object with some substructure and a spatial extent of  $\sim 2'$ , whereas in SDSS it appears as a collection of point-like sources. Intrigued by the likelihood that these compact sources are associated with the low sur-

face brightness object, we obtained follow-up spectroscopic observations of NGC1052–DF2 using the 10 m W. M. Keck Observatory. We also observed the galaxy with the Hubble Space Telescope (HST).

A color image generated from the HST  $V_{606}$  and  $I_{814}$  data is shown in Fig. 1. The galaxy has a striking appearance. In terms of its apparent size and surface brightness it resembles dwarf spheroidal galaxies such as those recently identified in the M101 group at 7 Mpc,<sup>8</sup> but the fact that it is only marginally resolved implies that it is at a much greater distance. Using the  $I_{814}$  band image we derive a surface brightness fluctuation distance of  $D_{\text{SBF}} = 19.0 \pm 1.7$  Mpc (see Methods). It is located only  $14'$  from the luminous elliptical galaxy NGC 1052, which has distance measurements ranging from 19.4 Mpc to 21.4 Mpc.<sup>9,10</sup> We infer that NGC1052–DF2 is associated with NGC 1052, and we adopt  $D \approx 20$  Mpc for the galaxy.

We parameterized the galaxy’s structure with a two-dimensional Sérsic profile.<sup>11</sup> The Sérsic index is  $n = 0.6$ , the axis ratio is  $b/a = 0.85$ , the central surface brightness is  $\mu(V_{606}, 0) = 24.4$  mag arcsec<sup>−2</sup>, and the effective radius along the major axis is  $R_e = 22.6''$ , or 2.2 kpc. We conclude that NGC1052–DF2 falls in the “ultra diffuse galaxy” (UDG) class,<sup>5</sup> which have  $R_e > 1.5$  kpc and  $\mu(g, 0) > 24$  mag arcsec<sup>−2</sup>. In terms of its structural parameters it is very similar to the galaxy Dragonfly 17 in the Coma cluster.<sup>5</sup> The total magnitude of NGC1052–DF2 is  $M_{606} = -15.4$ , and the total luminosity is  $L_V = 1.1 \times 10^8 L_{\odot}$ . Its color  $V_{606} - I_{814} = 0.37 \pm 0.05$  (AB), similar to that of other UDGs and metal-poor globular clusters.<sup>12</sup> The stellar mass was determined in two ways: by placing a stellar population at  $D = 20$  Mpc that matches the global properties of NGC1052–DF2 (see Methods), and by assuming  $M/L_V = 2.0$  as found for globular clusters.<sup>13</sup> Both methods give  $M_{\text{stars}} \approx 2 \times 10^8 M_{\odot}$ .

We obtained spectroscopy of objects in the NGC1052–DF2 field with the W. M. Keck Observatory. Details of the observations and data reduction are given in the Methods section. We find ten objects with a radial velocity close to  $1,800 \text{ km s}^{-1}$  (all other objects are Milky Way stars or background galaxies). We conclude that there is indeed a population of compact, luminous objects associated with NGC1052–DF2. Their spectra near the strongest Ca triplet (CaT) lines are shown in Fig. 2. The mean velocity of the ten objects is  $\langle v \rangle = 1,803_{-2}^{+2} \text{ km s}^{-1}$ . The NGC 1052 group

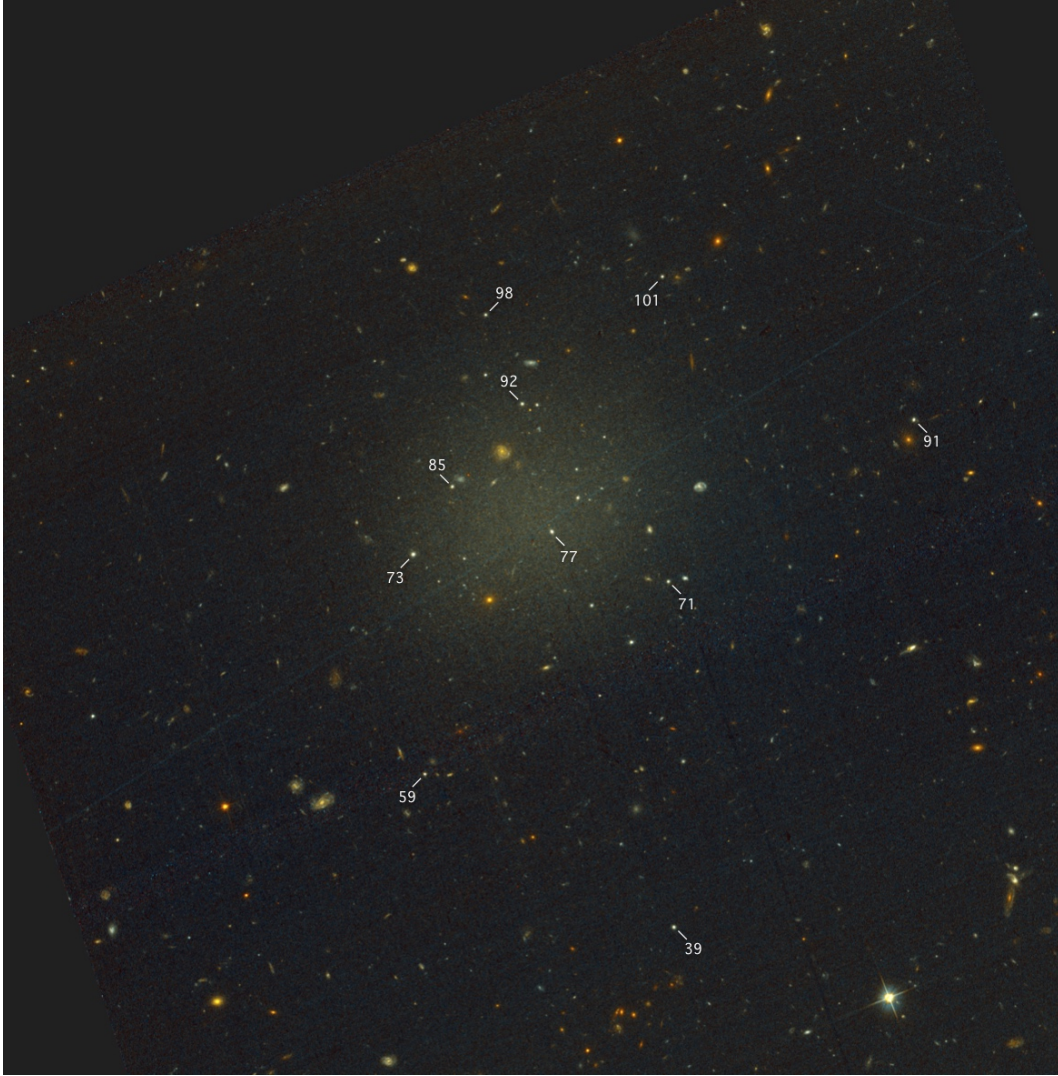


Figure 1: **HST/ACS image of NGC1052–DF2.** NGC1052–DF2 was identified as a large ( $\sim 2'$ ) low surface object, at  $\alpha = 2^h 41^m 46.8^s$ ;  $\delta = -8^\circ 24' 12''$  (J2000). Hubble Space Telescope imaging of NGC1052–DF2 was obtained 2016 November 10, using the Advanced Camera for Surveys (ACS). The exposure time was 2,180 s in the  $V_{606}$  filter and 2,320 s in the  $I_{814}$  filter. The image spans  $3.2' \times 3.2'$ , or  $18.6 \times 18.6$  kpc at the distance of NGC1052–DF2; North is up and East is to the left. Faint striping is caused by imperfect CTE removal. Ten spectroscopically-confirmed luminous compact objects are marked.

has a radial velocity of  $1,425 \text{ km s}^{-1}$ , with a  $1\sigma$  spread of only  $\pm 111 \text{ km s}^{-1}$  (based on 21 galaxies). NGC1052–DF2 has a peculiar velocity of  $+378 \text{ km s}^{-1}$  ( $3.4\sigma$ ) with respect to the group, and  $+293 \text{ km s}^{-1}$  with respect to NGC 1052 itself (Fig. 3).

Images of the compact objects are shown in Fig. 2 and their locations are marked on Fig. 1. Their spatial distribution is somewhat more extended than that of the smooth galaxy light: their half-number radius is  $R_{gc} \sim 3.1$  kpc (compared to  $R_e = 2.2$  kpc for the light) and the outermost object is at  $R_{out} = 7.6$  kpc. In this respect, and in their compact morphologies (they are just-resolved in our HST images, as expected for their distance) and colors, they are similar to globular clusters and we will refer to them as such.

However, their luminosities are much higher than those of typical globular clusters. The brightest (GC-73) has an absolute magnitude of  $M_{606} = -10.1$ , similar to that of the brightest globular cluster in the Milky Way ( $\omega$  Cen). Furthermore, the galaxy has no statistically-significant population of globular clusters near the canonical peak of the luminosity function at  $M_V \approx -7.5$ . The properties of these enigmatic objects are the subject of another paper (P.v.D. et al., in preparation).

The central observational result of the present study is the remarkably small spread among the velocities of the ten clusters (Fig. 3). The observed velocity dispersion is  $\sigma_{obs} = 8.4 \text{ km s}^{-1}$ , as measured with the biweight estimator (see Methods). This value is much smaller than that in

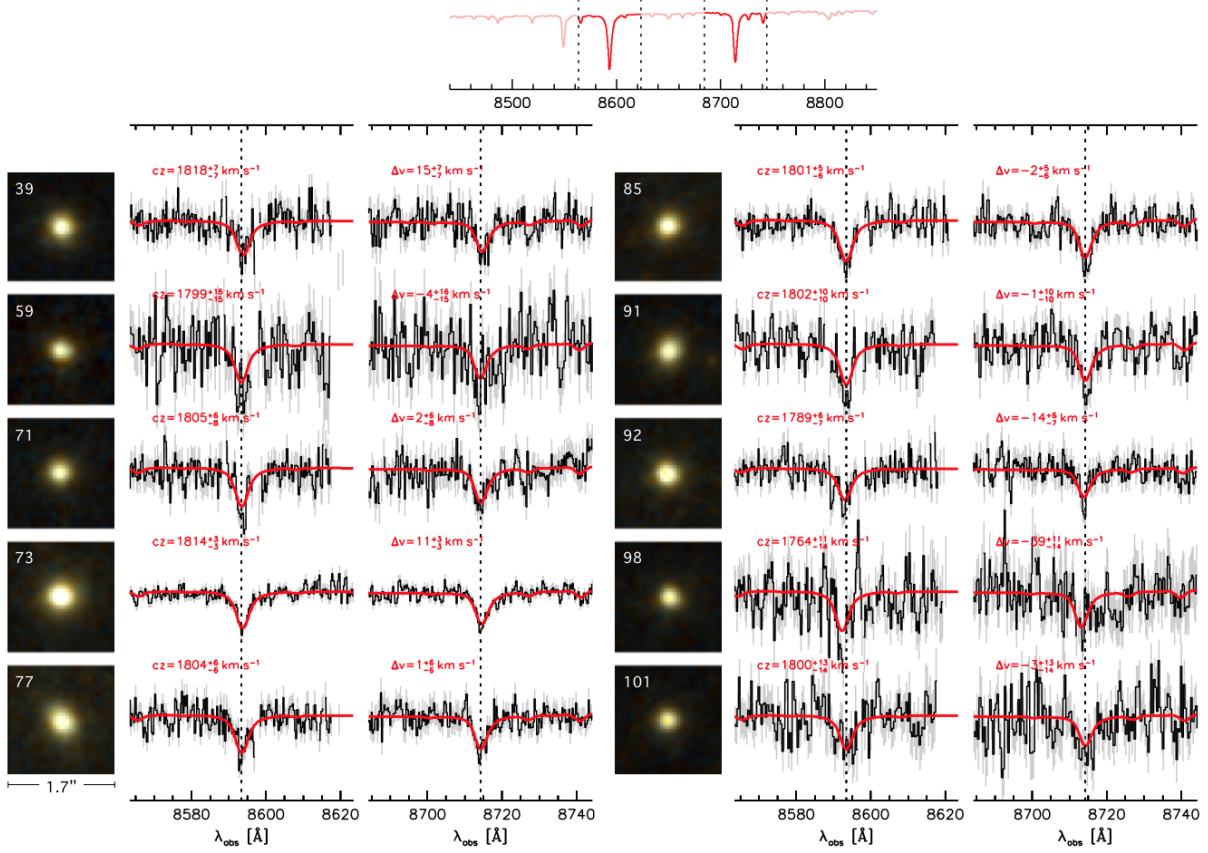


Figure 2: **Spectra of the compact objects.** The square panels show the HST/ACS images of the ten confirmed compact objects. Each panel spans  $1.7'' \times 1.7''$ , or  $165 \times 165$  pc at the distance of NGC1052–DF2. The Keck spectra are shown next to the corresponding HST images. The regions around the reddest  $\lambda 8544.4$ ,  $\lambda 8664.5$  Ca II triplet lines are shown, as illustrated in the model spectrum at the top; the  $\lambda 8500.4$  Calcium triplet line was included in the fit but falls on a sky line for the radial velocity of these objects. The spectra were obtained with LRIS, DEIMOS, or both. The spectral resolution is  $\sigma_{\text{instr}} \approx 30 \text{ km s}^{-1}$ . Uncertainties in the spectra are in grey. The signal-to-noise ratio ranges from  $3.4 \text{ pix}^{-1}$  to  $12.8 \text{ pix}^{-1}$ , with  $0.4 \text{ \AA}$  pixels. The red lines show the best-fitting models. Radial velocities  $c_z$  are indicated, as well as the velocity offset with respect to the central  $\langle v \rangle = 1803 \text{ km s}^{-1}$ . This velocity is indicated with dashed vertical lines.

previously studied (cluster) UDGs,<sup>12,18</sup> and not much higher than the expectation from observational errors alone. Taking the errors into account, we find an intrinsic dispersion of  $\sigma_{\text{intr}} = 3.2_{-3.2}^{+5.5} \text{ km s}^{-1}$ . The 90% confidence upper limit is  $\sigma_{\text{intr}} < 10.5 \text{ km s}^{-1}$ . To our knowledge this is the coolest known galaxy outside of the Local Group. Within the Local Group, typical galaxies with velocity dispersions in this range are small ( $R_e \sim 200$  pc) and have a low stellar mass ( $M_{\text{stars}} \sim 2 - 3 \times 10^6 M_{\odot}$ ).<sup>19</sup> The average velocity dispersion of Local Group galaxies with  $8.0 \leq \log(M/M_{\odot}) \leq 8.6$  is  $32 \text{ km s}^{-1}$  (dotted curve in Fig. 3a).

We calculate the corresponding 90% confidence upper limit on the mass of NGC1052–DF2 using the tracer mass estimator (TME) method,<sup>15</sup> which provides an estimate of the dynamical mass within the radius of the outermost discrete tracer. We find  $M_{\text{dyn}} < 3.4 \times 10^8 M_{\odot}$  within  $R_{\text{out}} = 7.6$  kpc. We also determine the dynamical mass within the projected half-number radius of the globular cluster system,<sup>16</sup> and find  $M_{\text{dyn}} < 3.2 \times 10^8 M_{\odot}$  within

$$R_{\text{gc}} = 3.1 \text{ kpc.}$$

In Fig. 4a the enclosed mass is compared to the expected mass from the stars alone (orange line) and to models with different halo masses. The dynamical mass is consistent with the stellar mass, leaving little room for dark matter. The best fit to the kinematics is obtained for  $M_{\text{halo}} = 0$ , and the 90% confidence upper limit on the dark matter halo mass is  $M_{\text{halo}} < 1.5 \times 10^8 M_{\odot}$ . We note that the combination of the large spatial extent and low dynamical mass of NGC1052–DF2 yields an unusually robust constraint on the total halo mass. Typically, kinematic tracers are only available out to a small fraction of  $R_{200}$ , and a large extrapolation is required to convert the measured enclosed mass to a total halo mass.<sup>4</sup> However, for a halo of mass  $M_{200} \sim 10^8 M_{\odot}$  the virial radius is only  $\sim 10$  kpc, similar to the radius where the outermost globular clusters reside. As shown in Fig. 4b, a galaxy with a stellar mass of  $M_{\text{stars}} = 2 \times 10^8 M_{\odot}$  is expected to have a halo mass of  $M_{\text{halo}} \approx 6 \times 10^{10} M_{\odot}$ , a factor of  $\sim 400$  higher than the upper limit that we derive. We conclude that

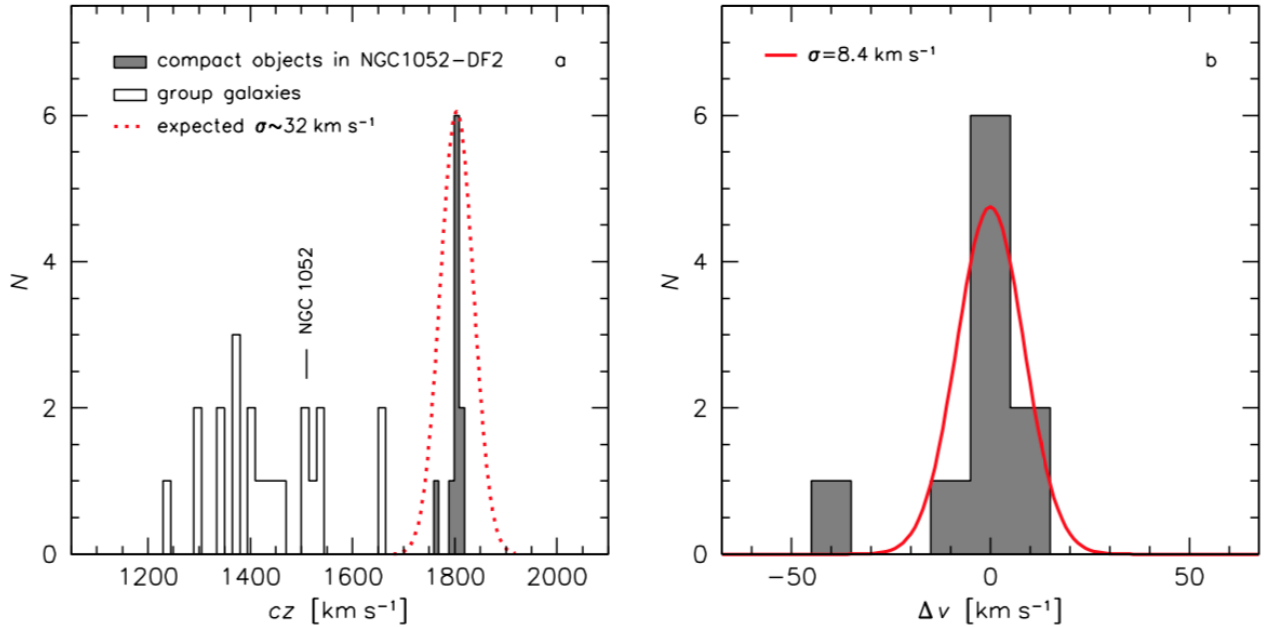


Figure 3: **Velocity dispersion.** The filled grey histograms show the velocity distribution of the ten compact objects. Panel a shows a wide velocity range, and includes the velocities of all 21 galaxies in the NASA/IPAC Extragalactic Database with  $cz < 2,500 \text{ km s}^{-1}$  that are within a projected distance of two degrees from NGC 1052. The red dotted curve shows a Gaussian with a width of  $\sigma = 32 \text{ km s}^{-1}$ , the average velocity dispersion of Local Group galaxies with  $8.0 \leq \log(M_{\text{stars}}/M_{\odot}) \leq 8.6$ . Panel b shows a narrow velocity range centered on  $cz = 1,803 \text{ km s}^{-1}$ . The red solid curve is a Gaussian with a width that is equal to the biweight dispersion of the velocity distribution of the compact objects,  $\sigma_{\text{obs}} = 8.4 \text{ km s}^{-1}$ . Taking observational errors into account, we derive an intrinsic dispersion of  $\sigma_{\text{intr}} = 3.2^{+5.5}_{-3.2} \text{ km s}^{-1}$ . The 90 % confidence upper limit on the intrinsic dispersion is  $\sigma_{\text{intr}} < 10.5 \text{ km s}^{-1}$ .

NGC1052–DF2 is extremely deficient in dark matter, and a good candidate for a “baryonic galaxy” with no dark matter at all.

It is unknown how the galaxy was formed. One possibility is that it is an old tidal dwarf, formed from gas that was flung out of merging galaxies. Its location near an elliptical galaxy and its high peculiar velocity are consistent with this idea. Its relatively blue color suggests a lower metallicity than might be expected for such objects,<sup>20</sup> but that depends on the detailed circumstances of its formation.<sup>21</sup> An alternative explanation is that the galaxy formed from low metallicity gas that was swept up in quasar winds.<sup>22</sup> The lack of dark matter, the location near a massive elliptical, the peculiar velocity, and the color are all qualitatively consistent with this scenario, although it is not clear whether the large size and low surface brightness of NGC1052–DF2 could have been produced by this process. A third option is that the galaxy formed from inflowing gas that fragmented before reaching NGC 1052, either relatively close to the assembling galaxy<sup>23</sup> or out in the halo.<sup>24</sup> This fragmentation may have been aided or precipitated by jet-induced shocks.<sup>25</sup> In any scenario the luminous globular cluster-like objects require an explanation; generically, it seems likely that the three peculiar aspects of the galaxy (its large size, its low dark matter content, and its population of luminous compact objects) are related.

An important missing piece of information is the number density of galaxies such as NGC1052–DF2. There are several other objects in our Cycle 24 HST program that look broadly similar, but these do not have dynamical measurements yet – and the fact that other UDGs have anomalously *high* dark matter fractions<sup>12,18</sup> demonstrates that such data are needed to interpret these galaxies.

Regardless of the formation history of NGC1052–DF2, its existence has implications for the dark matter paradigm. Our results demonstrate that dark matter is separable from galaxies, which is (under certain circumstances) expected if it is bound to baryons through nothing but gravity. The “bullet cluster” demonstrates that dark matter does not always trace the bulk of the baryonic mass,<sup>26</sup> which in clusters is in the form of gas. NGC1052–DF2 enables us to make the complementary point that dark matter does not always coincide with galaxies either: it is a distinct “substance” that may or may not be present in a galaxy. Furthermore, and paradoxically, the existence of NGC1052–DF2 may falsify alternatives to dark matter. In theories such as MOND<sup>27</sup> and the recently proposed emergent gravity paradigm<sup>28</sup> a “dark matter” signature should *always* be detected, as it is an unavoidable consequence of the presence of ordinary matter. In fact, it had been argued previously<sup>29</sup> that the apparent *absence* of galaxies such as NGC1052–DF2 constituted a falsi-

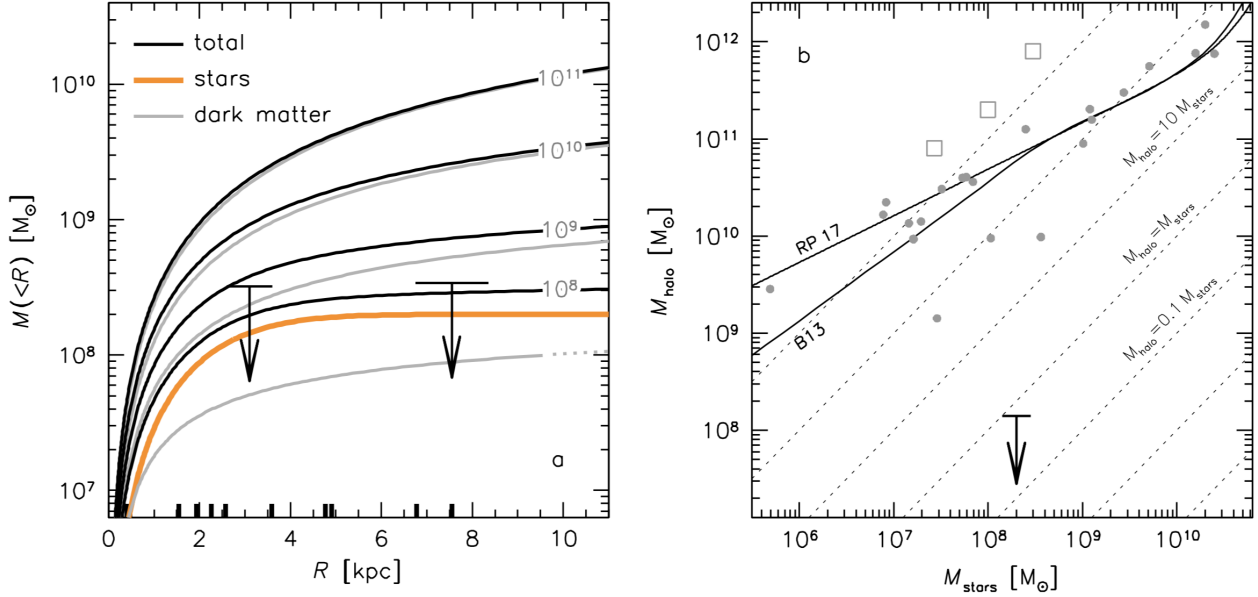


Figure 4: **Constraints on the halo mass.** Panel a shows enclosed mass profiles for NFW halos<sup>14</sup> of masses  $M_{200} = 10^8 M_{\odot}$ ,  $10^9 M_{\odot}$ ,  $10^{10} M_{\odot}$ , and  $10^{11} M_{\odot}$  (grey lines). The  $10^8 M_{\odot}$  halo profile is shown by a dotted line beyond  $R = R_{200} \sim 10$  kpc. The orange curve is the enclosed mass profile for the stellar component, and the black curves are the total mass profiles  $M_{\text{total}} = M_{\text{stars}} + M_{\text{halo}}$ . The ten globular clusters are at distances ranging from  $R = 0.4$  kpc to  $R = 7.6$  kpc; short vertical bars on the horizontal axis indicate the locations of individual clusters. The 90% upper limits on the total enclosed mass of NGC1052–DF2 are shown by arrows. The limit at  $R = 7.6$  kpc was determined with the TME method.<sup>15</sup> The arrow at  $R = 3.1$  kpc is the mass limit within the half-number radius of the globular cluster system.<sup>16</sup> The dynamical mass of NGC1052–DF2 is consistent with the stellar mass, and leaves little room for a dark matter halo. Panel b shows the upper limit on the halo mass, and compares this to the expected dark matter mass from studies that model the halo mass function and the evolution of galaxies.<sup>2,17</sup> Grey solid symbols are nearby dwarf galaxies with rotation curves extending to at least two disk scale lengths.<sup>4</sup> Open squares are three cluster UDGs with measured kinematics: VCC 1287,<sup>18</sup> Dragonfly 44,<sup>12</sup> and DFX1.<sup>12</sup> NGC1052–DF2 falls a factor of  $\gtrsim 400$  below the canonical relations.

fication of the standard cosmological model, and evidence for modified gravity. For a MOND acceleration scale of  $a_0 = 3.7 \times 10^3 \text{ km}^2 \text{ s}^{-2} \text{ kpc}^{-1}$  the expected<sup>30</sup> velocity dispersion of NGC1052–DF2 is  $\sigma_M \approx (0.05 GM_{\text{stars}} a_0)^{1/4} \approx 20 \text{ km s}^{-1}$ , a factor of two higher than the 90% upper limit on the observed dispersion.

## METHODS

**Imaging.** In this paper we use imaging from the Dragonfly Telephoto Array, the Sloan Digital Sky Survey, the MMT, the Gemini North telescope, and the Hubble Space Telescope.

**Dragonfly:** The Dragonfly Telephoto Array<sup>6</sup> data were obtained in the context of the Dragonfly Nearby Galaxy Survey.<sup>31</sup> Dragonfly was operating with 8 telephoto lenses at the time of the observations, forming the optical equivalent of an f/1.0 refractor with a 40 cm aperture. The data reach a  $1\sigma$  surface brightness limit of  $\mu(g) \sim 29 \text{ mag arcsec}^{-2}$  in  $12'' \times 12''$  boxes.<sup>31</sup> The full Dragonfly field is shown in Extended Data Figure 1, as well as the area around NGC 1052 and NGC1052–DF2.

**SDSS:** SDSS images in  $g$ ,  $r$ , and  $i$  were obtained from the

DR14 Sky Server.<sup>32</sup> To generate the image in Extended Data Figure 4 the data in the three bands were summed without weighting or scaling. The object is located near the corner of a frame. We note that the SDSS photometry for the compact objects is not reliable, as it is “contaminated” by the low surface brightness emission of the galaxy (which is just detected in SDSS).

**MMT:** MMT/Megacam imaging of the NGC 1052 field was available from a project to image the globular cluster systems of nearby early-type galaxies.<sup>33</sup> The data were taken in the  $r$  and  $i$  bands, in  $0.9''$  seeing. They were used for target selection in our first Keck spectroscopic run.

**Gemini:** We obtained imaging with the Gemini-North Multi Object Spectrograph<sup>34</sup> (GMOS) in program GN-2016B-DD-3. The observations were executed on 2016 October 10, with total exposure times of 3,000 s in the  $g$  band and 3,000 s in the  $i$  band. The seeing was  $0.65''$  in  $i$  and  $0.70''$  in  $g$ . The data were reduced using the Gemini IRAF package. Low order polynomials were fitted to individual (dithered) 300 s frames after carefully masking objects, to reduce large scale background gradients at low surface brightness levels. The images were used to aid in the target selection and mask design for the LRIS spectroscopy. The Gemini data also pro-

vide the best available information on the regularity of the galaxy at low surface brightness levels (see below). The combined frames still show some background artifacts but they are less prominent than those in the HST data. Finally, a visual inspection of the Gemini images prompted us to request a change in the scheduling of HST program GO-14644, moving the already-planned ACS observation of NGC1052–DF2 to an earlier date.

*HST:* The HST data were obtained as part of program GO-14644. The aim of this program is to obtain ACS images of a sample of 23 low surface brightness objects that were identified in fields of the Dragonfly Nearby Galaxy Survey.<sup>31</sup> NGC1052–DF2 was observed on 2016 November 16, for a total of two orbits. Exposure times were 2,180 s in  $V_{606}$  and 2,320 s in  $I_{814}$ . In this paper we use drizzled .drc images, which have been corrected for charge transfer efficiency (CTE) effects. Despite this correction some CTE artifacts are still visible in the data (see Fig. 1).

**Structural parameters.** The size, surface brightness, and other structural parameters of NGC1052–DF2 were determined from the HST data. First, the  $I_{814}$  image was rebinned to a lower resolution to increase the S/N ratio per pixel. Then, a preliminary object mask was created from a segmentation map produced by SExtractor,<sup>35</sup> using a relatively high detection threshold. A first-pass Sérsic model<sup>36</sup> for the galaxy was obtained using the GALFIT software.<sup>11</sup> This model was subtracted from the data, and an improved object mask was created using a lower SExtractor detection threshold. Finally, GALFIT was run again to obtain the final structural parameters and total magnitude. The total magnitude in the  $V_{606}$  band, and the  $V_{606} - I_{814}$  color, were determined by running GALFIT on the (binned and masked)  $V_{606}$  image with all parameters except the total magnitude fixed to the  $I_{814}$  values. The structural parameters, total magnitude, and color are listed in the main text. We note that we measured nearly identical structural parameters from the Gemini images.

**Spectroscopy.** We obtained spectroscopy of compact objects in the NGC1052–DF2 field in two observing runs. The first set of observations was obtained on 2016 September 28 with the Deep Imaging Multi-Object Spectrograph<sup>37</sup> (DEIMOS) on Keck II, and the second was obtained on 2016 October 26 and 27 with the Low-Resolution Imaging Spectrometer<sup>38</sup> (LRIS) on Keck I.

*DEIMOS observations:* Conditions were variable, with cirrus clouds increasing throughout the night. We obtained 4 hrs of total on-source exposure time on a single multi-object mask; a second mask was exposed but yielded no useful data due to clouds. The target selection algorithm gave priority to compact objects with  $i \lesssim 22.5$  near NGC1052–DF2, selected from the MMT data. We used the 1,200 lines  $\text{mm}^{-1}$  grating with a slit width of  $0.75''$ , providing an instrumental resolution of  $\sigma_{\text{instr}} \approx 25 \text{ km s}^{-1}$ . The data were reduced with the same pipeline that we used

previously<sup>12,39</sup> for the Coma UDGs Dragonfly 44 and DFX1. The globular clusters GC-39, GC-71, GC-73, GC-77, GC-85, GC-92, and GC-98 (see Fig. 1 and 2) were included in this mask.

*LRIS observations:* Two multi-slit masks were observed, one for 3.5 hrs (on source) on October 26 and a second for 4 hrs on October 27. Targets were selected from the Gemini data, giving priority to compact objects that had not been observed with DEIMOS. Conditions were fair during both nights, with intermittent cirrus and seeing of  $\approx 1''$ . We used the 1,200 lines  $\text{mm}^{-1}$  gold coated grating blazed at  $9,000 \text{ \AA}$ . The instrumental resolution  $\sigma_{\text{instr}} \approx 30 \text{ km s}^{-1}$ . A custom pipeline was used for the data reduction, modeled on the one that we developed for DEIMOS. LRIS suffers from significant flexure, and the main difference with the DEIMOS pipeline is that each individual 1800 s exposure was reduced and calibrated independently to avoid smoothing of the combined spectra in the wavelength direction. The clusters GC-39, GC-59, GC-73, GC-91, and GC-101 were included in the first mask; GC-39, GC-71, GC-77, GC-85, and GC-92 were included in the second.

*Combined spectra:* Most compact objects were observed multiple times, and we combined these individual spectra to increase the S/N ratio. All spectra were given equal weight, and prior to combining they were divided by a low order polynomial fit to the continuum in the CaT region. We tested that weighting by the formal S/N ratio instead does not change the best-fit velocities. The individual spectra were also shifted in wavelength to account for the heliocentric correction; this needs to be done at this stage as the DEIMOS and LRIS data were taken one month apart. Six GCs have at least two independent observations and effective exposure times of  $\approx 8$  hrs; four were observed only once: GC-59, GC-91, GC-98, and GC-101. The S/N ratio in the final spectra ranges from 3–4  $\text{pix}^{-1}$  for GC-59, GC-98, and GC-101 to 13  $\text{pix}^{-1}$  for GC-73. A pixel is  $0.4 \text{ \AA}$ , or  $14 \text{ km s}^{-1}$ .

**Velocity measurements.** Radial velocities were determined for all objects with detected CaT absorption lines. No fits were attempted for background galaxies (based on the detection of redshifted emission lines), Milky Way stars, or spectra with no visible features. The measurements were performed by fitting a template spectrum to the observations, using the emcee MCMC algorithm.<sup>40</sup> The template is a high resolution stellar population synthesis model,<sup>41</sup> smoothed to the instrumental resolution. The model has an age of 11 Gyr and a metallicity of  $[\text{Fe}/\text{H}] = -1$ , which is consistent with the colors of the compact objects ( $V_{606} - I_{814} \sim 0.35$ ); the results are independent of the precise choice of template. The fits are performed over the observed wavelength range  $8,530 \text{ \AA} \leq \lambda \leq 8,750 \text{ \AA}$  and have three free parameters: the radial velocity, the normalization, and an additive term that serves as a template mismatch parameter (as it allows the strength of the absorption lines to vary with respect to the continuum). The fit was performed twice. After the first

pass all pixels that deviate  $> 3\sigma$  are masked in the second fit. This step reduces the effect of systematic sky subtraction residuals on the fit.

The uncertainties given by the `emcee` method do not take systematic errors into account. Following previous studies<sup>42</sup> we determined the uncertainties in the velocities by shuffling the residuals. For each spectrum, the best-fitting model was subtracted from the data. Next, 500 realizations of the data were created by randomizing the wavelengths of the residual spectra and then adding the shuffled residuals to the best-fitting model. These 500 spectra were then fit using a simple  $\chi^2$  minimization, and the 16<sup>th</sup> and 84<sup>th</sup> percentiles of the resulting velocity distribution yield the error bars. In order to preserve the higher noise at the location of sky lines the randomization was done separately for pixels at the locations of sky lines and for pixels in between the lines. We find that the resulting errors show the expected inverse trend with the S/N ratio of the spectra, whereas the `emcee` errors show large variation at fixed S/N ratio.

We tested the reliability of the errors by applying the same procedure to the individual LRIS and DEIMOS spectra for the six objects that were observed with both instruments (GC-39, GC-71, GC-73, GC-77, GC-85, and GC-92). For each object the observed difference between the LRIS and DEIMOS velocities was divided by the expected error in the difference. The rms of these ratios is  $1.2 \pm 0.3$ , that is, the empirically-determined uncertainties are consistent with the observed differences between the independently-measured LRIS and DEIMOS velocities.

**Velocity dispersion.** The observed velocity distribution of the ten clusters is not well approximated by a Gaussian. Six of the ten have velocities that are within  $\pm 4 \text{ km s}^{-1}$  of the mean and one is  $39 \text{ km s}^{-1}$  removed from the mean. As a result, different ways to estimate the Gaussian-equivalent velocity spread  $\sigma_{\text{obs}}$  yield different answers. The normalized median absolute deviation  $\sigma_{\text{obs,nmad}} = 4.7 \text{ km s}^{-1}$ , the biweight<sup>43</sup>  $\sigma_{\text{obs,bi}} = 8.4 \text{ km s}^{-1}$ , and the rms  $\sigma_{\text{obs,rms}} = 14.3 \text{ km s}^{-1}$ . The rms is driven by one object with a relatively large velocity uncertainty (GC-98), and is inconsistent with the velocity distribution of the other nine. Specifically, for 10 objects drawn from a Gaussian distribution and including the observed errors the probability of measuring  $\sigma_{\text{bi}} \leq 8.4$  if  $\sigma_{\text{rms}} \geq 14.3$  is 1.5%, and the probability of measuring  $\sigma_{\text{nmad}} \leq 4.7$  is  $3 \times 10^{-3}$ . We therefore adopt the biweight dispersion rather than the rms when determining the intrinsic dispersion below. We then show that the presence of GC-98 is consistent with the intrinsic dispersion that we derive using this statistic.

The observed dispersion has to be corrected for observational errors, which are of the same order as  $\sigma_{\text{obs}}$  itself. We determined the intrinsic dispersion and its uncertainty in the following way. For a given value of  $\sigma_{\text{test}}$  we generated 1000

samples of 10 velocities, distributed according to a Gaussian of width  $\sigma_{\text{test}}$ . The ten velocities in each sample were then perturbed with errors, drawn from Gaussians with widths equal to the empirically-determined uncertainties in the measured dispersions. Using the biweight estimator, “measured” dispersions  $\sigma_{\text{obs,test}}$  were calculated for all samples. If the value 8.4 is within the 16<sup>th</sup> – 84<sup>th</sup> percentile of the distribution of  $\sigma_{\text{obs,test}}$  then  $\sigma_{\text{test}}$  is within the  $\pm 1\sigma$  uncertainty on  $\sigma_{\text{intr}}$ . This method gives  $\sigma_{\text{intr}} = 3.2^{+5.5}_{-3.2} \text{ km s}^{-1}$ . As the intrinsic dispersion is consistent with zero, a more meaningful number than the best-fit is the 90% confidence upper limit; we find  $\sigma_{\text{intr}} < 10.5 \text{ km s}^{-1}$ .

We now return to the question whether GC-98 is consistent with the other nine objects. This cluster has a velocity offset of  $\Delta v = -39^{+11}_{-14} \text{ km s}^{-1}$ . For the upper limit on the intrinsic dispersion ( $\sigma_{\text{intr}} = 10.5 \text{ km s}^{-1}$ ) the object is a  $2.4\sigma$  outlier, and the probability of having a  $> 2.4\sigma$  outlier in a sample of ten is 15%. Interestingly the combination of the biweight constraint of  $\sigma_{\text{intr}} < 10.5$  and the existence of GC-98 implies a fairly narrow range of intrinsic dispersions that are consistent with the entire set of ten velocities (assuming that they are drawn from a Gaussian distribution and the errors are correct). The probability of having at least one object with the velocity of GC-98 is  $< 10\%$  if the intrinsic dispersion is  $\sigma_{\text{intr}} < 8.8 \text{ km s}^{-1}$ . Taking both 90% confidence limits at face value, the allowed range in the intrinsic dispersion is  $8.8 \text{ km s}^{-1} < \sigma_{\text{intr}} < 10.5 \text{ km s}^{-1}$ .

**Expected dispersion from Local Group galaxies.** In Fig. 3a we illustrate how unusual the kinematics of NGC1052–DF2 are by comparing the observed velocity distribution to that expected from Local Group galaxies with the same stellar mass (broken red curve). The width of this Gaussian was calculated from the SEPT2015 version of the Nearby Dwarf Galaxies catalog.<sup>19</sup> The catalog has entries for both velocity dispersions and rotation velocities, and for both gas and stars. To obtain a homogeneous estimate we use “effective” dispersions,  $\sigma_{\text{eff}} \equiv (\sigma^2 + 0.5v_{\text{rot}}^2)^{0.5}$ . When both gas and stellar kinematics are available we use the highest value of  $\sigma_{\text{eff}}$ , as this typically is a rotation curve measurement from gas at large radii versus a stellar velocity dispersion measurement. Stellar masses were calculated directly from the *V* band absolute magnitude assuming  $M/L_V = 2.0$ , for consistency with NGC1052–DF2. Five galaxies have a stellar mass that is within a factor of two of that of NGC1052–DF2: IC 1613, NGC 6822, Sextans B, and the M31 satellites NGC 147 and NGC 185. The average dispersion of these five galaxies is  $\langle \sigma_{\text{eff}} \rangle = 32 \text{ km s}^{-1}$ , with an rms variation of  $8 \text{ km s}^{-1}$ .

In Extended Data Figure 2 we compare NGC1052–DF2 to the nearby dwarf sample in the plane of velocity dispersion versus half-light radius, with the size of the symbols indicating the stellar mass. Comparing NGC1052–DF2 to other galaxies with velocity dispersions in this range, we find

that its size is larger by a factor of  $\sim 10$  and its stellar mass is larger by a factor of  $\sim 100$ .

**Distance.** The heliocentric radial velocity of NGC1052–DF2 is  $1,803 \pm 2 \text{ km s}^{-1}$ , or  $1,748 \pm 16 \text{ km s}^{-1}$  after correcting for the effects of the Virgo cluster, the great attractor, and the Shapley supercluster on the local velocity field.<sup>44</sup> For  $H_0 = 70 \pm 3 \text{ km s}^{-1} \text{ Mpc}^{-1}$  a Hubble flow distance of  $D_{\text{HF}} = 25 \pm 1 \text{ Mpc}$  is obtained. However, the proximity to NGC 1052 ( $14'$ , or  $\approx 80 \text{ kpc}$  in projection) strongly suggests that NGC1052–DF2 is associated with this massive elliptical galaxy. The distance to NGC 1052, as determined from surface brightness fluctuations and the fundamental plane,<sup>9,10</sup> is  $D_{1052} = 20.4 \pm 1.0 \text{ Mpc}$ . The velocity of NGC1052–DF2 with respect to NGC 1052 is then  $+293 \text{ km s}^{-1}$ .

A third distance estimate can be obtained from the luminosity function of the compact objects. As discussed in another paper (P.v.D. et al., in preparation) the luminosity function has a narrow peak at  $m_V \approx 22.0$ . The canonical globular cluster luminosity function can be approximated by a Gaussian with a well-defined peak<sup>45</sup> at  $M_V \approx -7.5$ . If the compact objects are typical globular clusters, the implied distance is  $D_{\text{GC}} \approx 8 \text{ Mpc}$ . This is an important possibility, as the main conclusions of the paper would be weakened considerably if the galaxy is so close to us. For this distance the stellar mass estimate is an order of magnitude lower:  $M_{\text{stars}} \approx 3 \times 10^7 M_{\odot}$ . The four Local Group galaxies that have a stellar mass within a factor of two of this value (Fornax, Andromeda II, Andromeda VII, and UGC 4879) have a mean dispersion of  $\langle \sigma_{\text{eff}} \rangle = 11.7 \pm 0.5 \text{ km s}^{-1}$ , only slightly higher than the upper limit to the dispersion of NGC1052–DF2. The peculiar velocity of the galaxy would be  $\sim 1200 \text{ km s}^{-1}$ ; this is of course extreme, but it is difficult to argue that it is less likely than having a highly peculiar globular cluster population and a lack of dark matter.

Fortunately, we have independent information to verify the distance, namely the appearance of NGC1052–DF2 in the HST images. In Extended Data Figure 3a we show the central  $33'' \times 33''$  of the galaxy in the HST  $I_{814}$  band. A smooth model of the galaxy, obtained by median filtering the image, was subtracted; background galaxies and globular clusters were masked. The mottled appearance is not due to noise but due to the variation in the number of giants contributing to each pixel. Following previous studies,<sup>9,46,47</sup> we measure the surface brightness fluctuation (SBF) signal from this image and determine the distance from the SBF magnitude.

The azimuthally-averaged power spectrum of the image is shown in Extended Data Figure 3b. As is customary<sup>46</sup> the smallest and largest wavenumbers are omitted, as they are dominated by, respectively, residual large scale structure in the image and noise correlations. Again following previous studies,<sup>46,47</sup> the power spectrum is fit by a combination of

a constant (dotted line) and the expectation power spectrum  $E(k)$  (dashed line). The expectation power spectrum is the convolution of the power spectrum of the PSF and that of the window function. The window function is the square root of the median-filtered model of the galaxy, multiplied by the mask containing the globular clusters and background galaxies.

The normalization of  $E(k)$  is the SBF magnitude,  $\overline{m}_{814}$ . We find  $\overline{m}_{814} = 29.45 \pm 0.10$ . Using Eq. 2 in ref. 47,  $V_{606} - I_{814} = 0.37 \pm 0.05$ , and  $g_{475} - I_{814} = 1.852(V_{606} - I_{814}) + 0.096$ , the absolute SBF magnitude is  $M_{814} = -1.94 \pm 0.17$ . The uncertainty is a combination of the error in the  $V_{606} - I_{814}$  color and the systematic uncertainty in the extrapolation of the relation between  $g_{475} - I_{814}$  color and  $M_{814}$  (as determined from the difference between Eqs. 1 and 2 in ref. 47). The SBF distance modulus  $\overline{m} - \overline{M} = 31.39 \pm 0.20$ , and the SBF distance  $D_{\text{SBF}} = 19.0 \pm 1.7 \text{ Mpc}$ . This result is consistent with  $D_{1052}$ , and rules out the “globular cluster distance” of  $D_{\text{GC}} = 8 \text{ Mpc}$ .

**Stellar mass.** We determined the stellar mass from a stellar population synthesis model.<sup>41</sup> A two-dimensional model galaxy was created using the ArtPop code<sup>48</sup> that matches the morphology, luminosity, color, and SBF signal of NGC1052–DF2. The model has a metallicity  $[Z/H] = -1$  and an age of 11 Gyr. These parameters are consistent with the regular morphology of the galaxy and with spectroscopic constraints on the stellar populations of Coma cluster UDGs.<sup>49</sup> For a Kroupa IMF<sup>50</sup> the stellar mass of this model is  $1.8 \times 10^8 M_{\odot}$ , similar to that obtained from a simple  $M/L_V = 2.0$  conversion<sup>13</sup> ( $M_{\text{stars}} = 2.2 \times 10^8 M_{\odot}$ ). In the main text and below we assume  $M_{\text{stars}} \approx 2 \times 10^8 M_{\odot}$ . We note that the uncertainty in the stellar mass is much smaller than that in the dynamical mass, for reasonable choices of the IMF.

**Dynamical equilibrium.** Some large low surface brightness objects are almost certainly in the process of disruption; examples are the “star pile” in the galaxy cluster Abell 545,<sup>51,52</sup> the boomerang-shaped galaxy DF4 in the field of M101,<sup>53</sup> and And XIX in the Local Group<sup>54</sup> (marked in Extended Data Figure 2). And XIX, and also And XXI and And XXV, are particularly informative as they combine large sizes with low velocity dispersions,<sup>55</sup> and it has been suggested that tidal interactions have contributed to their unusual properties.<sup>54</sup> (We note that these galaxies are not direct analogs of NGC1052–DF2: the stellar masses of these Andromeda satellites are a factor of  $\sim 100$  lower than that of NGC1052–DF2, and their dynamical  $M/L$  ratios are at least a factor of 10 higher.) In Extended Data Figure 4c we show the Gemini  $i$  band image of NGC1052–DF2 (along with the Dragonfly and SDSS images). There is no convincing evidence of strong position angle twists or tidal features at least out to  $R \sim 2R_e$  (see also the Dragonfly image in panel a). The regular appearance strongly suggests that the object has



survived in its present form for multiple dynamical times, and we infer that the kinematics can likely be interpreted in the context of a system that is in dynamical equilibrium.

We note that the regular morphology of NGC1052–DF2 also provides an interesting constraint on its formation time: the orbital velocity in the outer parts is  $\gtrsim 5$  Gyr, which means it has to have formed very early in order to lose any sign of its assembly. Furthermore, it provides a lower limit for the 3D distance between NGC1052–DF2 and the massive elliptical galaxy NGC 1052. The Jacobi radius (i.e., the distance from the center of the galaxy to the first Lagrangian point) is given by<sup>56</sup>

$$R_J = \left( \frac{GM}{2V_{1052}^2} \right)^{1/3} R_{1052}^{2/3}, \quad (1)$$

with  $R_{1052}$  the distance between NGC1052–DF2 and NGC 1052 and  $V_{1052}$  the circular velocity of NGC 1052. Taking  $R_J > 5$  kpc,  $M \sim 2 \times 10^8 M_\odot$ , and  $V_{1052} \sim 300 \text{ km s}^{-1}$  (the velocity difference between the two galaxies, as well as  $\sim \sqrt{2}\sigma_{1052}$ ), we obtain  $R_{1052} \gtrsim 160$  kpc, a factor of two larger than the projected distance.

**Source of dynamical support.** The morphology of the galaxy strongly indicates that it is supported by random motions rather than rotation: the Sérsic index is 0.6, similar to that of dSph galaxies; the isophotes are elliptical rather than disky; and there are no bars, spiral arms, or other features that might be expected in a thin disk. The galaxy has not been detected in moderately deep H I observations.<sup>57</sup> It is also difficult to imagine a physical model for the formation of a huge, extremely thin disk of massive blue globular clusters, even in spiral galaxies: although the kinematics of the metal-rich globular cluster population in M31 are clearly related to its disk, the metal-poor ones have a large velocity dispersion.<sup>58</sup> Finally, there is no evidence for a velocity gradient. In Extended Data Figure 5a we show the measured velocities of the globular clusters as a function of the projected distance along the major axis. There is no coherent pattern. Based on these arguments our default mass measurement assumes that the galaxy is supported by random motions.

**Dynamical mass measurement.** Following a previous study of the kinematics of globular clusters in a UDG,<sup>18</sup> we use the tracer mass estimator (TME) to determine the dynamical mass. This method was developed to determine the enclosed mass from an ensemble of discrete tracers, such as satellite galaxies or globular clusters.<sup>15,59</sup> The mass within the distance of the outermost object is given by

$$M_{\text{TME}} = \frac{C}{G} \langle v^2 r^\alpha \rangle r_{\text{out}}^{1-\alpha}, \quad (2)$$

with  $v$  the velocities of individual clusters with respect to the mean,  $r$  the projected distances of the clusters from the center of the galaxy,  $r_{\text{out}}$  the distance of the furthest cluster,

and  $\alpha$  the slope of the potential (with density  $\rho \propto r^{-(\alpha+2)}$ ). For the case  $\alpha = 1$  the potential is similar to that of a point mass,  $\alpha = 0$  corresponds to  $\rho \propto r^{-2}$  and a flat rotation curve, and for  $\alpha = -1$  the density  $\rho \propto r^{-1}$ . Equation 2 does not take observational errors or outliers into account; we therefore introduce the modified expression

$$M_{\text{TME}} \approx \frac{C}{G} \left[ S_{\text{bi}}(v_{\text{intr}} r^{\alpha/2}) \right]^2 r_{\text{out}}^{1-\alpha}. \quad (3)$$

Here observational errors are taken into account by setting  $v_{\text{intr}} = f^{-1}(\Delta v_{\text{obs}})$ , with  $\Delta v_{\text{obs}}$  listed in Fig. 2 and  $f^{-1} = \sigma_{\text{intr}}/\sigma_{\text{obs}}$ .  $S_{\text{bi}}(x)$  denotes the biweight estimator of the width of the distribution. Note that Eq. 3 reduces to  $M_{\text{TME}} = (C/G)\sigma_{\text{intr}}^2 r_{\text{out}}$  for  $\alpha = 0$ . The constant  $C$  is given by

$$C = \frac{4\Gamma\left(\frac{\alpha}{2} + \frac{5}{2}\right)}{\sqrt{\pi}\Gamma\left(\frac{\alpha}{2} + 1\right)} \frac{\alpha + \gamma + 1 - 2\beta}{\alpha + 3 - \beta(\alpha + 2)}, \quad (4)$$

with  $\gamma$  the power-law slope of the density profile of the clusters,  $\beta = 1 - \sigma_t^2/\sigma_r^2$  the Binney anisotropy parameter, and  $\Gamma(x)$  the gamma function. We determine the 3D density profile from a powerlaw fit to the distribution of the spectroscopically-confirmed globular clusters, finding  $\gamma = 0.9 \pm 0.3$ .

For an isothermal velocity dispersion profile ( $\alpha = 0$ ) and isotropic orbits ( $\beta = 0$ ) we determine  $M_{\text{TME}} < 3.4 \times 10^8 M_\odot$  at 90 % confidence. The results are not very sensitive to the assumed slope of the potential or moderate anisotropy. Changing  $\alpha$  to 1 or  $-1$  reduces the mass by 10 % or 20 % respectively. Tangential anisotropy with  $\sigma_t^2 = 2\sigma_r^2$  increases the mass limit to  $M_{\text{TME}} < 4.2 \times 10^8 M_\odot$ ; radial anisotropy with  $\sigma_t^2 = 0.5\sigma_r^2$  yields  $M_{\text{TME}} < 2.4 \times 10^8 M_\odot$ . We also consider errors in the density profile of the globular clusters; for  $\gamma = 0.5$  the mass decreases by 20 % and for  $\gamma = 1.5$  the mass increases by 30 %.

**Robustness tests.** As a test of the robustness of our results we consider three alternative mass estimates. The first is the dynamical mass within the half-number radius of the globular cluster system.<sup>16</sup> This mass estimate does not extend as far in radius as the TME method but is less sensitive to the assumed level of anisotropy. For  $R_{\text{gc}} = 3.1$  kpc and  $\sigma_{\text{intr}} < 10.5 \text{ km s}^{-1}$  we find  $M_{\text{dyn}} < 3.2 \times 10^8 M_\odot$  (see Fig. 4). As the halo profile is still rising at  $R = 3.1$  kpc the constraint on the halo mass is weaker than our default value, and we find  $M_{\text{halo}} < 8 \times 10^8 M_\odot$ .

The second test replaces  $\sigma_{\text{bi}}$  with  $\sigma_{\text{rms}}$ , even though the rms is driven by a single cluster (GC-98) and the velocity distribution of the other nine objects is inconsistent with this. The observed rms is  $\sigma_{\text{obs,rms}} = 14.3 \text{ km s}^{-1}$ , or  $\sigma_{\text{intr,rms}} = 12.2 \text{ km s}^{-1}$  after taking observational errors into account. The implied TME mass is  $M_{\text{dyn}} \approx 5 \times 10^8 M_\odot$ , and the halo mass  $M_{\text{halo}} \approx 3 \times 10^8 M_\odot$ .

The third test sets the arguments against a disk aside and assumes that the observed velocities reflect rotation in an inclined, infinitely-thin disk. The axis ratio of NGC1052–DF2 is  $b/a = 0.85 \pm 0.02$ , which means that the inclination-corrected velocities are a factor of  $(\sin(\cos^{-1}(b/a)))^{-1} \approx 1.9$  higher than the observed ones. Assuming an (unphysical) disk dispersion of  $0 \text{ km s}^{-1}$ , the inclination-corrected rotation velocity would be  $v_{\text{rot}} \approx 1.4 \times 3.2 \times 1.9 = 9_{-9}^{+14} \text{ km s}^{-1}$ , where it is assumed that the rotation velocity is approximately 1.4 times the line-of-sight velocity dispersion.<sup>60,61</sup> The enclosed mass within  $R = 7.6 \text{ kpc}$  would be  $M_{\text{disk}} = 1.4_{-1.4}^{+7.6} \times 10^8 M_{\odot}$ .

For all these mass estimates the implied ratio  $M_{\text{halo}}/M_{\text{stars}} \lesssim 4$ , the lowest ratio measured for any galaxy and two orders of magnitude below the canonical stellar mass – halo mass relation.

**Data availability.** The HST data are available in the Mikulski Archive for Space Telescopes (MAST; <http://archive.stsci.edu>), under program ID 14644. All other data that support the findings of this study are available from the corresponding author upon reasonable request.

**Code availability.** We have made use of standard data reduction tools in the IRAF and Python environments, and the publicly available codes SExtractor,<sup>35</sup> GALFIT,<sup>11</sup> and emcee.<sup>40</sup>

- 
1. Moster, B. P. *et al.* Constraints on the Relationship between Stellar Mass and Halo Mass at Low and High Redshift. *ApJ* **710**, 903–923 (2010).
  2. Behroozi, P. S., Wechsler, R. H. & Conroy, C. The Average Star Formation Histories of Galaxies in Dark Matter Halos from  $z = 0-8$ . *ApJ* **770**, 57 (2013).
  3. More, S. *et al.* Satellite kinematics - III. Halo masses of central galaxies in SDSS. *MNRAS* **410**, 210–226 (2011).
  4. Oman, K. A. *et al.* Missing dark matter in dwarf galaxies? *MNRAS* **460**, 3610–3623 (2016).
  5. van Dokkum, P. G. *et al.* Forty-seven Milky Way-sized, Extremely Diffuse Galaxies in the Coma Cluster. *ApJ* **798**, L45 (2015).
  6. Abraham, R. G. & van Dokkum, P. G. Ultra-Low Surface Brightness Imaging with the Dragonfly Telephoto Array. *PASP* **126**, 55–69 (2014).
  7. Karachentsev, I. D., Karachentseva, V. E., Suchkov, A. A. & Grebel, E. K. Dwarf galaxy candidates found on the SERC EJ sky survey. *A&AS* **145**, 415–423 (2000).
  8. Danieli, S. *et al.* The Dragonfly Nearby Galaxies Survey. III. The Luminosity Function of the M101 Group. *ApJ* **837**, 136 (2017).
  9. Tonry, J. L. *et al.* The SBF Survey of Galaxy Distances. IV. SBF Magnitudes, Colors, and Distances. *ApJ* **546**, 681–693 (2001).
  10. Blakeslee, J. P., Lucey, J. R., Barris, B. J., Hudson, M. J. & Tonry, J. L. A synthesis of data from fundamental plane and surface brightness fluctuation surveys. *MNRAS* **327**, 1004–1020 (2001).
  11. Peng, C. Y., Ho, L. C., Impey, C. D. & Rix, H.-W. Detailed Structural Decomposition of Galaxy Images. *AJ* **124**, 266–293 (2002).
  12. van Dokkum, P. *et al.* Extensive Globular Cluster Systems Associated with Ultra Diffuse Galaxies in the Coma Cluster. *ApJ* **844**, L11 (2017).
  13. McLaughlin, D. E. & van der Marel, R. P. Resolved Massive Star Clusters in the Milky Way and Its Satellites: Brightness Profiles and a Catalog of Fundamental Parameters. *ApJS* **161**, 304–360 (2005).
  14. Navarro, J. F., Frenk, C. S. & White, S. D. M. A Universal Density Profile from Hierarchical Clustering. *ApJ* **490**, 493–508 (1997).
  15. Watkins, L. L., Evans, N. W. & An, J. H. The masses of the Milky Way and Andromeda galaxies. *MNRAS* **406**, 264–278 (2010).

16. Wolf, J. *et al.* Accurate masses for dispersion-supported galaxies. *MNRAS* **406**, 1220–1237 (2010).
17. Rodríguez-Puebla, A., Primack, J. R., Avila-Reese, V. & Faber, S. M. Constraining the galaxy-halo connection over the last 13.3 Gyr: star formation histories, galaxy mergers and structural properties. *MNRAS* **470**, 651–687 (2017).
18. Beasley, M. A. *et al.* An Overmassive Dark Halo around an Ultra-diffuse Galaxy in the Virgo Cluster. *ApJ* **819**, L20 (2016).
19. McConnachie, A. W. The Observed Properties of Dwarf Galaxies in and around the Local Group. *AJ* **144**, 4 (2012).
20. Bournaud, F. *et al.* Missing Mass in Collisional Debris from Galaxies. *Science* **316**, 1166 (2007).
21. Ploekinger, S. *et al.* Tidal dwarf galaxies in cosmological simulations. *MNRAS* **474**, 580–596 (2018).
22. Natarajan, P., Sigurdsson, S. & Silk, J. Quasar outflows and the formation of dwarf galaxies. *MNRAS* **298**, 577–582 (1998).
23. Canning, R. E. A. *et al.* Filamentary star formation in NGC 1275. *MNRAS* **444**, 336–349 (2014).
24. Mandelker, N., van Dokkum, P. G., Brodie, J. P. & Ceverino, D. Cold filamentary accretion and the formation of metal poor globular clusters. *ApJ* **000**, 000–000 (2017).
25. van Breugel, W., Filippenko, A. V., Heckman, T. & Miley, G. Minkowski’s object - A starburst triggered by a radio jet. *ApJ* **293**, 83–93 (1985).
26. Clowe, D. *et al.* A Direct Empirical Proof of the Existence of Dark Matter. *ApJ* **648**, L109–L113 (2006).
27. Milgrom, M. A modification of the Newtonian dynamics as a possible alternative to the hidden mass hypothesis. *ApJ* **270**, 365–370 (1983).
28. Verlinde, E. P. Emergent Gravity and the Dark Universe. *ArXiv e-prints* (2016).
29. Kroupa, P. The Dark Matter Crisis: Falsification of the Current Standard Model of Cosmology. *PASA* **29**, 395–433 (2012).
30. Angus, G. W. Dwarf spheroidals in MOND. *MNRAS* **387**, 1481–1488 (2008).
31. Merritt, A., van Dokkum, P., Abraham, R. & Zhang, J. The Dragonfly nearby Galaxies Survey. I. Substantial Variation in the Diffuse Stellar Halos around Spiral Galaxies. *ApJ* **830**, 62 (2016).
32. Abolfathi, B. *et al.* The Fourteenth Data Release of the Sloan Digital Sky Survey: First Spectroscopic Data from the extended Baryon Oscillation Sky Survey and from the second phase of the Apache Point Observatory Galactic Evolution Experiment. *ArXiv e-prints* (2017).
33. Napolitano, N. R. *et al.* The Planetary Nebula Spectrograph elliptical galaxy survey: the dark matter in NGC 4494. *MNRAS* **393**, 329–353 (2009).
34. Hook, I. M. *et al.* The Gemini-North Multi-Object Spectrograph: Performance in Imaging, Long-Slit, and Multi-Object Spectroscopic Modes. *PASP* **116**, 425–440 (2004).
35. Bertin, E. & Arnouts, S. SExtractor: Software for source extraction. *A&AS* **117**, 393–404 (1996).
36. Sersic, J. L. *Atlas de galaxias australes* (Cordoba, Argentina: Observatorio Astronomico, 1968, 1968).
37. Faber, S. M. *et al.* The DEIMOS spectrograph for the Keck II Telescope: integration and testing. In Iye, M. & Moorwood, A. F. M. (eds.) *Instrument Design and Performance for Optical/Infrared Ground-based Telescopes*, vol. 4841 of *Proc. SPIE*, 1657–1669 (2003).
38. Oke, J. B. *et al.* The Keck Low-Resolution Imaging Spectrometer. *PASP* **107**, 375 (1995).
39. van Dokkum, P. *et al.* A High Stellar Velocity Dispersion and ~100 Globular Clusters for the Ultra-diffuse Galaxy Dragonfly 44. *ApJ* **828**, L6 (2016).
40. Foreman-Mackey, D., Hogg, D. W., Lang, D. & Goodman, J. emcee: The MCMC Hammer. *PASP* **125**, 306–312 (2013).
41. Conroy, C., Gunn, J. E. & White, M. The Propagation of Uncertainties in Stellar Population Synthesis Modeling. I. The Relevance of Uncertain Aspects of Stellar Evolution and the Initial Mass Function to the Derived Physical Properties of Galaxies. *ApJ* **699**, 486–506 (2009).
42. van Dokkum, P. G., Kriek, M. & Franx, M. A high stellar velocity dispersion for a compact massive galaxy at redshift  $z = 2.186$ . *Nature* **460**, 717–719 (2009).
43. Beers, T. C., Flynn, K. & Gebhardt, K. Measures of location and scale for velocities in clusters of galaxies - A robust approach. *AJ* **100**, 32–46 (1990).
44. Mould, J. R. *et al.* The Hubble Space Telescope Key Project on the Extragalactic Distance Scale. XXVIII. Combining the Constraints on the Hubble Constant. *ApJ* **529**, 786–794 (2000).
45. Rejkuba, M. Globular cluster luminosity function as distance indicator. *Ap&SS* **341**, 195–206 (2012).
46. Mei, S. *et al.* The Advanced Camera for Surveys Virgo Cluster Survey. V. Surface Brightness Fluctuation Calibration for Giant and Dwarf Early-Type Galaxies. *ApJ* **625**, 121–129 (2005).
47. Blakeslee, J. P. *et al.* Surface Brightness Fluctuations in the Hubble Space Telescope ACS/WFC F814W Bandpass and an Update on Galaxy Distances. *ApJ* **724**, 657–668 (2010).
48. Danieli, S., van Dokkum, P. & Conroy, C. Hunting Faint Dwarf Galaxies in the Field Using Integrated Light Surveys. *ArXiv e-prints* (2017).
49. Gu, M. *et al.* Low Metallicities and Old Ages for Three Ultra-Diffuse Galaxies in the Coma Cluster. *ArXiv e-prints* (2017).

50. Kroupa, P. On the variation of the initial mass function. *MNRAS* **322**, 231–246 (2001).
51. Struble, M. F. Optical discovery of intracluster matter on the Palomar Observatory Sky Survey - The star pile in A545. *ApJ* **330**, L25–L28 (1988).
52. Salinas, R. *et al.* Crazy heart: kinematics of the “star pile” in Abell 545. *A&A* **528**, A61 (2011).
53. Merritt, A. *et al.* The Dragonfly Nearby Galaxies Survey. II. Ultra-Diffuse Galaxies near the Elliptical Galaxy NGC 5485. *ApJ* **833**, 168 (2016).
54. Collins, M. L. M. *et al.* A Kinematic Study of the Andromeda Dwarf Spheroidal System. *ApJ* **768**, 172 (2013).
55. Tollerud, E. J. *et al.* The SPLASH Survey: Spectroscopy of 15 M31 Dwarf Spheroidal Satellite Galaxies. *ApJ* **752**, 45 (2012).
56. Baumgardt, H., Parmentier, G., Gieles, M. & Vesperini, E. Evidence for two populations of Galactic globular clusters from the ratio of their half-mass to Jacobi radii. *MNRAS* **401**, 1832–1838 (2010).
57. McKay, N. P. F. *et al.* The discovery of new galaxy members in the NGC 5044 and 1052 groups. *MNRAS* **352**, 1121–1134 (2004).
58. Caldwell, N. & Romanowsky, A. J. Star Clusters in M31. VII. Global Kinematics and Metallicity Subpopulations of the Globular Clusters. *ApJ* **824**, 42 (2016).
59. Bahcall, J. N. & Tremaine, S. Methods for determining the masses of spherical systems. I - Test particles around a point mass. *ApJ* **244**, 805–819 (1981).
60. Franx, M. What is the connection between ellipticals and bulges? In Dejonghe, H. & Habing, H. J. (eds.) *Galactic Bulges*, vol. 153 of *IAU Symposium*, 243 (1993).
61. Kochanek, C. S. The dynamics of luminous galaxies in isothermal halos. *ApJ* **436**, 56–66 (1994).

**Author Information** The authors declare that they have no competing financial interests. Correspondence and requests for materials should be addressed to P.v.D. (email: pieter.vandokkum@yale.edu).

**Acknowledgements** A.J.R. was supported by National Science Foundation grant AST-1616710 and as a Research Corporation for Science Advancement Cottrell Scholar. Based on observations obtained with the W. M. Keck Observatory on Mauna Kea, Hawaii. The authors wish to recognize and acknowledge the very significant cultural role and reverence that the summit of Mauna Kea has always had within the indigenous Hawaiian community. We are most fortunate to have the opportunity to conduct observations from this mountain.

**Author Contributions** P.v.D. led the observations, data reduction, and analysis, and wrote the manuscript. S.D. visually identified the galaxy in the Dragonfly data and created the model galaxies to determine the distance. Y.C. measured the structural parameters of the object. A.M. used an automated approach to verify the visual detections of low surface brightness galaxies in the Dragonfly data. J.Z. and A.M. reduced the Dragonfly data. E.O.S. provided the MMT image. All authors contributed to aspects of the analysis, and to the writing of the manuscript.

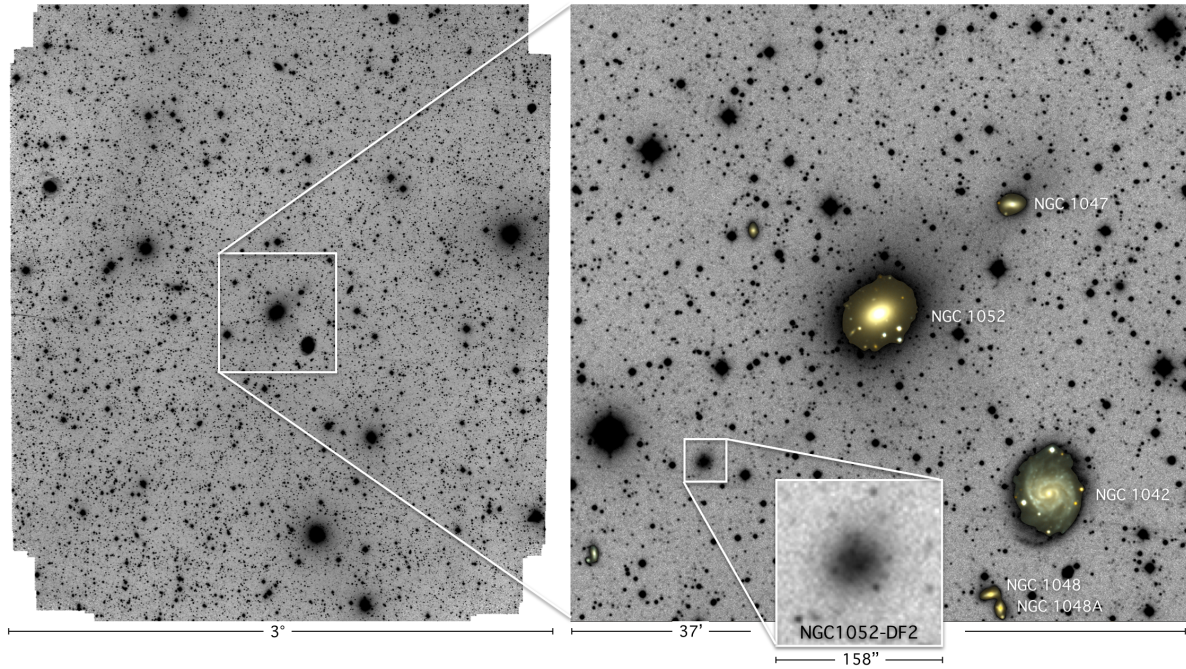


Figure Extended Data Figure 1: **NGC1052-DF2 in the Dragonfly field.** The full  $\sim 11$  degree<sup>2</sup> Dragonfly field centered on NGC 1052. The zoom-in shows the immediate surroundings of NGC 1052, with NGC1052-DF2 highlighted in the inset.

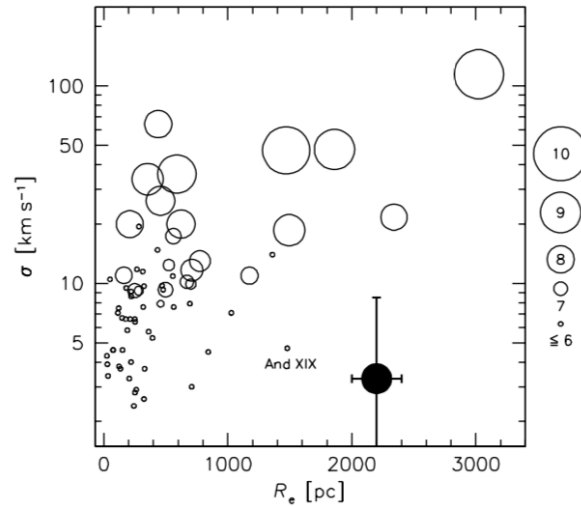


Figure Extended Data Figure 2: **Comparison to Local Group galaxies.** Open symbols are galaxies from the Nearby Dwarf Galaxies catalog<sup>19</sup> and the solid symbol with errorbars is NGC1052-DF2. The size of each symbol indicates the logarithm of the stellar mass, as shown in the legend. There are no galaxies in the Local Group that are similar to NGC1052-DF2. Galaxies with a similar velocity dispersion are a factor of  $\sim 10$  smaller and have stellar masses that are a factor of  $\sim 100$  larger. The labeled object (And XIX) is an Andromeda satellite that is thought to be in the process of tidal disruption.<sup>54</sup>

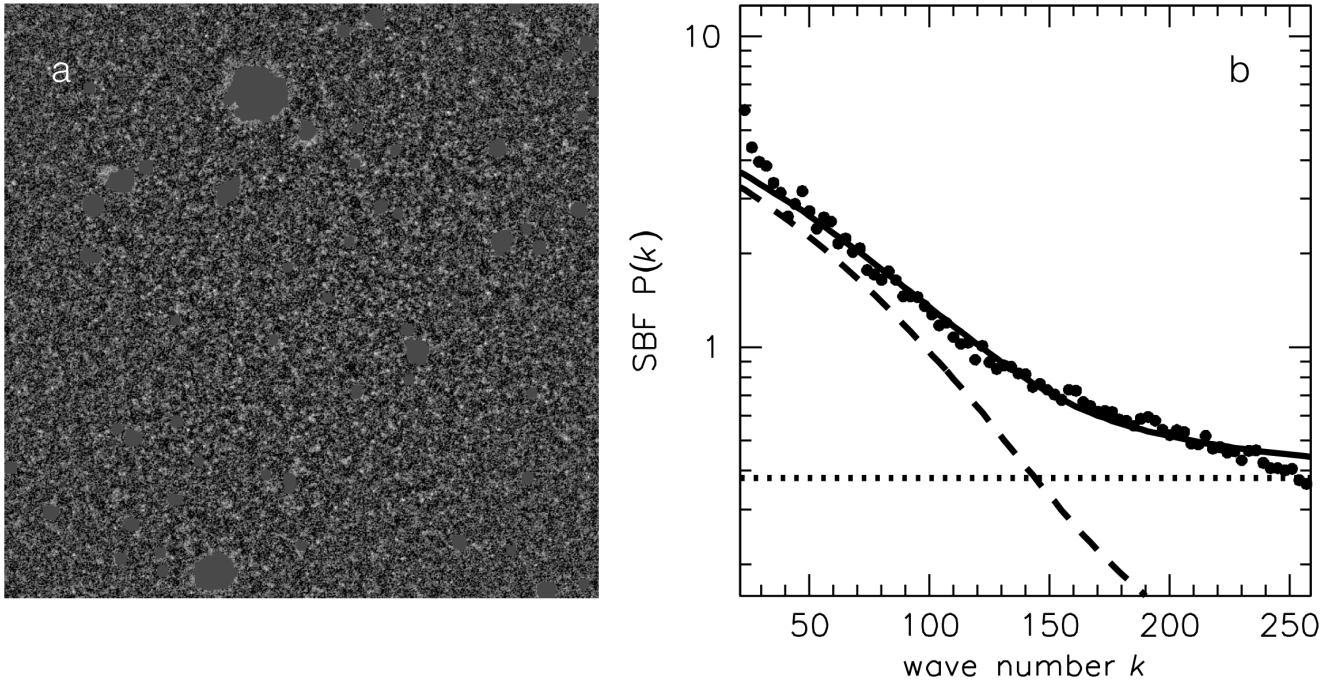


Figure Extended Data Figure 3: **Surface brightness fluctuation analysis.** We use the surface brightness fluctuation (SBF) signal in the HST  $I_{814}$  band to constrain the distance to NGC1052–DF2. Panel a shows the galaxy after subtracting a smooth model and masking background galaxies and globular clusters. The image spans  $33'' \times 33''$ . Panel b shows the azimuthally-averaged power spectrum. Following previous studies,<sup>9,46,47</sup> the power spectrum is fit by a combination of a constant (dotted line) and an expectation power spectrum  $E(k)$  (dashed line). From the normalization of  $E(k)$  we find that the SBF magnitude  $\bar{m}_{814} = 29.45 \pm 0.10$ . The implied distance is  $D_{\text{SBF}} = 19.0 \pm 1.7$  Mpc, consistent with the 20 Mpc distance of the luminous elliptical galaxy NGC 1052.

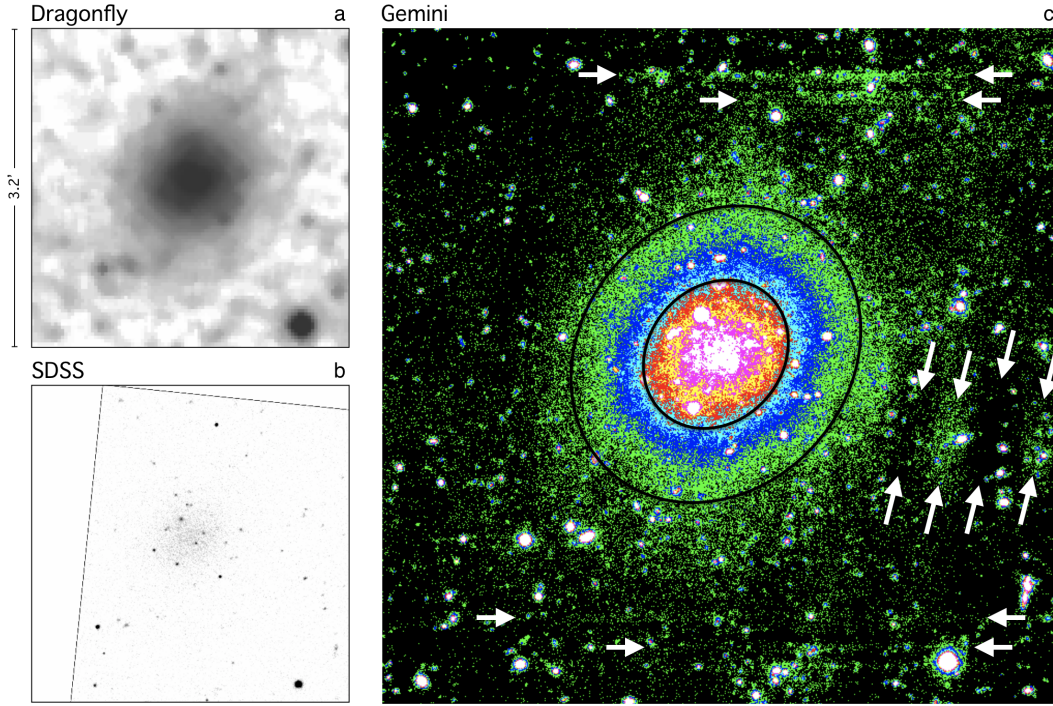


Figure Extended Data Figure 4: **Morphological coherence.** Panel a shows the sum of  $g$  and  $r$  images taken with the Dragonfly Telephoto Array. The image was smoothed by a  $10'' \times 10''$  median filter to bring out faint emission. The lowest surface brightness levels visible in the image are  $\approx 29 \text{ mag arcsec}^{-2}$ . Panel b shows a sum of SDSS  $g$ ,  $r$ , and  $i$  images. In SDSS the overdensity of compact objects stands out. Panel c shows the Gemini-North  $i$  band image of NGC1052-DF2, which provides the best information on the morphology of the galaxy. Black ellipses mark  $R = R_e$  and  $R = 2R_e$ . White arrows mark the most obvious reduction artifacts. The galaxy is regular out to at least  $R \sim 2R_e$ , with a well-defined center and a position angle and axis ratio that do not vary strongly with radius.

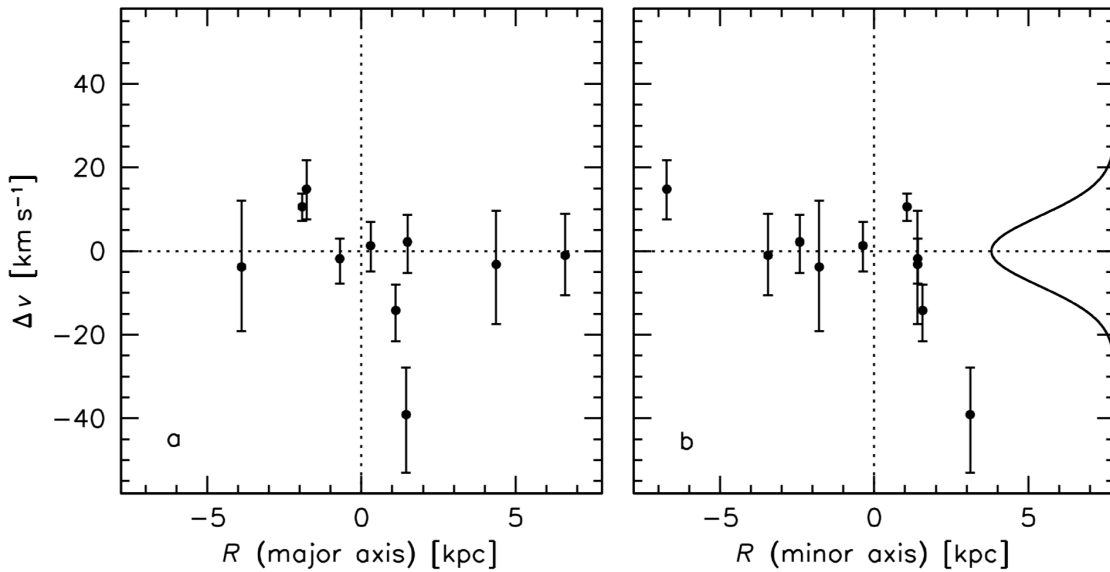


Figure Extended Data Figure 5: **Are the globular clusters in a thin rotating disk?** The two panels show the globular cluster velocities as a function of projected position along the major axis (panel a) and minor axis (panel b). Error bars are 1 s.d. There is no evidence for any trends. For reference, a Gaussian with  $\sigma = 8.4 \text{ km s}^{-1}$  is shown in panel b.